Modification of Plasma Membrane Organization in Tobacco Cells Elicited by Cryptogein[1][W]

Patricia Gerbeau-Pissot*, Christophe Der, Dominique Thomas, Iulia-Andra Anca, Kevin Grosjean, Yann Roche, Jean-Marie Perrier-Cornet, Sébastien Mongrand, and Françoise Simon-Plas

Université de Bourgogne (P.G.-P., C.D., D.T., K.G.), and Institut National de la Recherche Agronomique (I.-A.A., Y.R., F.S.-P.), Unité Mixte de Recherche 1347 Agroécologie, Equipe de Recherche Labelisée 6300 Centre National de la Recherche Scientifique, BP 86510, F–21000 Dijon, France; AgroSup Dijon, Laboratoire Procédés Alimentaires et Microbiologiques, F–21000 Dijon, France (J.-M.P.-C.); and Centre National de la Recherche Scientifique, Laboratoire de Biogenèse Membranaire, Unité Mixte de Recherche 5200, Université Victor Segalen, Institut National de la Recherche Agronomique Bordeaux Aquitaine, BP 81, F–33883 Villenave d'Ornon, France (S.M.)

Lipid mixtures within artificial membranes undergo a separation into liquid-disordered and liquid-ordered phases. However, the existence of this segregation into microscopic liquid-ordered phases has been difficult to prove in living cells, and the precise organization of the plasma membrane into such phases has not been elucidated in plant cells. We developed a multispectral confocal microscopy approach to generate ratiometric images of the plasma membrane surface of Bright Yellow 2 tobacco (*Nicotiana tabacum*) suspension cells labeled with an environment sensitive fluorescent probe. This allowed the in vivo characterization of the global level of order of this membrane, by which we could demonstrate that an increase in its proportion of ordered phases transiently occurred in the early steps of the signaling triggered by cryptogein and flagellin, two elicitors of plant defense reactions. The use of fluorescence recovery after photobleaching revealed an increase in plasma membrane fluidity induced by cryptogein, but not by flagellin. Moreover, we characterized the spatial distribution of liquid-ordered phases on the membrane of living plant cells and monitored their variations induced by cryptogein elicitation. We analyze these results in the context of plant defense signaling, discuss their meaning within the framework of the "membrane raft" hypothesis, and propose a new mechanism of signaling platform formation in response to elicitor treatment.

The adaptive capacity of biological membranes is a primary determinant of cell survival in fluctuating conditions. In particular, membrane physical properties are adjusted in the perception of and response to environmental modifications (including temperature, mechanical, and osmotic stresses) in various organisms (Los and Murata, 2004; Vígh et al., 2007; Verstraeten et al., 2010), including plants (Vaultier et al., 2006; Königshofer et al., 2008). Moreover, it has been shown that modifications of plasma membrane (PM) physical properties induced by pharmacological treatments can trigger signaling events in tobacco (*Nicotiana tabacum*) suspension cells (Bonneau et al., 2010). This reinforces the need to analyze the relationships between membrane organization and signaling in greater detail.

Fluidity, a physical property of the PM, is a measure of the rotational and translational motions of molecules within the membrane, and consequently this reflects the level of lipid order in the bilayer. Lipid order is comprised of structure, microviscosity, and membrane phase; the latter feature includes lipid shape, packing, and curvature (Rilfors et al., 1984; van der Meer et al., 1984; Bloom et al., 1991). Lipid self-association induces a physical segregation into lipid bilayers, wherein a liquid-ordered (Lo) phase coexists with a liquid-disordered (Ld) phase (Veatch and Keller, 2005; Gaus et al., 2006; Klymchenko et al., 2009; Heberle et al., 2010). The Lo phase couples a high rotational mobility with a high conformational order in the lipid acyl chain, two physical properties that could be spatially resolved by fluorescence microscopy (Kubiak et al., 2011). Moreover, some observations indicate that Lo size or proportion could be controlled by temperature or cholesterol content (Roche et al., 2008; Orth et al., 2011).

This preferential association of some lipids in complex mixtures has resulted in the "membrane raft" hypothesis within the cell biology field. This theory postulates the existence of small (20–200 nm), short-lived, sterol-, and sphingolipid-enriched Lo assemblies within the membrane. An important feature is that these aggregations are believed to coalesce, upon a biological stimulus, into larger structures whose dynamics can regulate many cellular processes (Simons and Ikonen, 1997; Pike,

2006; Lingwood and Simons, 2010; Simons and Gerl, 2010). An increased resistance to solubilization by detergents of Lo versus Ld phases has led researchers to consider that membrane fractions insoluble to nonionic detergents at low temperatures could contain the putative "raft" fractions. One caveat of this theory is that recovered detergent-insoluble membrane fractions (DIMs) only exist after detergent treatment and do not correspond to the native membrane structure (Lichtenberg et al., 2005). Nevertheless, their significant enrichment in sterols, sphingolipids, and specific subsets of proteins, some of which displaying a clustered distribution within the PM (Simons and Gerl, 2010), has encouraged their use as a biochemical counterpart of Lo microdomains existing in biological membranes.

Plant DIMs with a lipid content similar to animal DIMs have been isolated from several species, including tobacco cells, and are enriched in proteins involved in signaling and stress responses (Mongrand et al., 2004; Borner et al., 2005; Morel et al., 2006; Lefebvre et al., 2007; Kierszniowska et al., 2009). Moreover, immunoelectron microscopy experiments have revealed that lateral segregation of lipids and proteins occurs at the nanoscale level at the tobacco PM, thus correlating detergent insolubility with membrane domain localization of presumptive raft proteins (Raffaele et al., 2009; Furt et al., 2010; Demir et al., 2013). Together, these data point to the existence of specialized lipid domains in plants. Concomitantly, the presence of sterol-rich Lo membrane domains was observed in vivo at the tip of the growing pollen tube in *Picea meyeri*, using both filipin and the fluorescent probe 1-[2-hydroxy-3-(*N*,*N*-dimethyl-*N*-hydroxyethyl)ammoniopropyl]-4-[*β*-[2-(di-*n*-butylamino)-6-napthyl]vinyl] pyridinium dibromide (di-4-ANEPPDHQ; Liu et al., 2009). This observation argues in favor of a sterol-dependent organization of ordered domains at the plant PM surface. In addition, the combined use of fluorescent lipid analogs and the environmental dye laurdan has revealed different lipid phases that emerge in the PM of Arabidopsis (*Arabidopsis thaliana*) protoplasts during restoration of the cell wall (Blachutzik et al., 2012). Despite these details, necessary data concerning the presence and in vivo characterization of Lo domains at a micrometer to nanometer scale are still lacking.

The importance of a more refined resolution for observing Lo domains was proposed in several recent reviews (Bagatolli, 2006; Duggan et al., 2008; García-Sáez and Schwille, 2010; Owen et al., 2010a; Stöckl and Herrmann, 2010; Klenerman et al., 2011). Although the physical properties of biological membranes have been studied in situ by various techniques, including two-channel ratiometric microscopy (Owen et al., 2010c) and microscopy imaging of partitioning of fluorescent lipids and proteins (Rosetti et al., 2010) or environmentally sensitive probes (Parasassi et al., 1990; Jin et al., 2006), membrane segregation into microscopic Lo- and Ld-like phases has been difficult to observe in living cells. Furthermore, only a few studies have demonstrated that a microscopic phase separation involving an ordered phase similar to the Lo domain of model membranes could occur in biomembranes using PM giant vesicles (Baumgart et al., 2007; Lingwood et al., 2008; Sengupta et al., 2008). A potentially powerful approach for imaging small ordered membrane domains relies on environment-sensitive probes coupled with fluorescence spectroscopy (Gaus et al., 2003, 2006; Oncul et al., 2010). In particular, analysis of the fluorescence of the di-4-ANEPPDHQ probe, which exhibits an emission shift independent of local chemical composition under different lipid packing conditions (Jin et al., 2005; Demchenko et al., 2009; Dinic et al., 2011), recently enabled the imaging of plant membrane domains at the micrometer scale (Liu et al., 2009). The relevance of this approach has been confirmed by mapping membrane domains using generalized anisotropy-based images of di-4-ANEPPDHQ-stained T cell immunological synapses (Owen et al., 2010c), together with the characterization of membrane organization of nonadherent cells (such as living zebrafish embryo tissues) labeled with this dye (Owen et al., 2012a).

The function of dynamic PM compartmentalization in the detection and transduction of environmental signals in plant cells has only recently begun to emerge, along with a crucial role for sterols in this organization (for review, see Zappel and Panstruga, 2008; Mongrand et al., 2010; Simon-Plas et al., 2011). These observations make it indispensable to align how the surface membrane of living cells might reorganize during signaling with the membrane raft hypothesis. To investigate possible modifications of membrane organization during the initial steps of plant defense signaling, tobacco cells were treated with two well-described elicitors of defense reaction, cryptogein, a small protein able to trigger an hypersensitive reaction (HR) and an acquired resistance in tobacco plants (Ponchet et al., 1999; Garcia Brugger et al., 2006) together with a widely described signaling cascade in tobacco suspension cells, and flg22 (a 22-amino acid peptide corresponding to a conserved domain of bacterial flagellin). The latter peptide is also a potent elicitor in plants, yet it does not induce an HR type of necrosis (Gomez-Gomez and Boller, 2002; Chinchilla et al., 2007). The study of cryptogein response reveals that the earliest steps of the signal transduction pathway mainly involve PM activities (Ponchet et al., 1999; Garcia-Brugger et al., 2006). How the PM is laterally organized and possibly reorganized in response to this stress so it can efficiently trigger a signaling cascade remains unknown.

Here, we have developed a confocal multispectral microscopy approach to generate in vivo ratiometric pictures of large areas of the tobacco cell PM labeled with di-4-ANEPPDHQ, allowing the in vivo characterization of the global level of order of this membrane. Although an increase in the proportion of ordered phase within the membrane transiently occurred in the early steps of the cryptogein and flg22 signaling cascades, the fluorescence recovery after photobleaching (FRAP) technique revealed an increase in PM fluidity induced by cryptogein, but not by flagellin. Moreover,

we characterized the spatial distribution of Lo phases on the membrane of living plant cells and monitored the variations induced by cryptogein elicitation. The results are discussed within the framework of the "membrane raft" hypothesis, in which we propose a new mechanism of signaling platform formation in the context of plant defense.

RESULTS

Characterization of PM Order Level in Living Tobacco Cells

Tobacco suspension cells were stained for 1 min with the dye di-4-ANEPPDHQ (3 μM). No cell autofluorescence could be observed by confocal microscopy at an excitation of 488 nm and in the whole di-4-ANEPPDHQ emission spectrum (520–680 nm). Following addition of the dye, homogeneous labeling was exclusively observed at the PM for the duration of the experiment, indicating that di-4-ANEPPDHQ fluorescence is directly and fully related to PM organization (Supplemental Fig. S1). Emission fluorescence intensity of a single nonadherent living cell was recorded by focusing on its membrane surface plane (Supplemental Fig. S2), which allowed acquisition of a large surface area whose range varied from 30 to 500 μm^2 depending on cell size and shape (Fig. 1A). Central sections of the PM surface area were analyzed to avoid edge effects (Supplemental Fig. S3A).

The order level of the membrane revealed by di-4-ANEPPDHQ fluorescence is commonly quantified using the ratio of the emission fluorescence intensities recovered at 660 and 550 nm (I660/I550 nm; Jin et al., 2005; Roche et al., 2008, 2010; Dinic et al., 2011)). To generate ratiometric data, the fluorescence was captured simultaneously at different wavelengths using 32 independent photodetectors. This separation of the fluorescence of each channel (Fig. 1B) enabled us to precisely plot the di-4-ANEPPDHQ emission spectrum distributed from 520 to 680 nm (Fig. 1C). The two band-pass filters, 545 to 565 nm and 635 to 655 nm (Fig. 1C), correspond to the smallest interval (respectively closed to 550 and 660 nm) that yields a signal at least 10 times higher than the background. After dividing the resulting emission intensity of the two band-pass filters by one another, a red/green ratio (referred to as the red/green ratio of the membrane [RGM]; Supplemental Fig. S3B) of 0.94 ± 0.02 (SE of the mean; $n = 66$ cells) was measured for the PM of tobacco suspension cells. This RGM value is situated between 0.4 and 2, which are values observed respectively for Lo and Ld domains of 1,2-dipalmitoyl-sn-glycero-3-phosphocholine (DPPC)/1,2-dioleoyl-sn-glycero-3-phosphocholine (DOPC)/cholesterol giant vesicles (Jin et al., 2006). This ratio is also consistent with other reports in living cells, such as a value less than 1.5 for pollen tubes (Liu et al., 2009) and close to 0.6 in polarized neutrophil (Jin et al., 2006).

A cold temperature-induced blue shift in di-4-ANEPPDHQ emission spectra has been previously
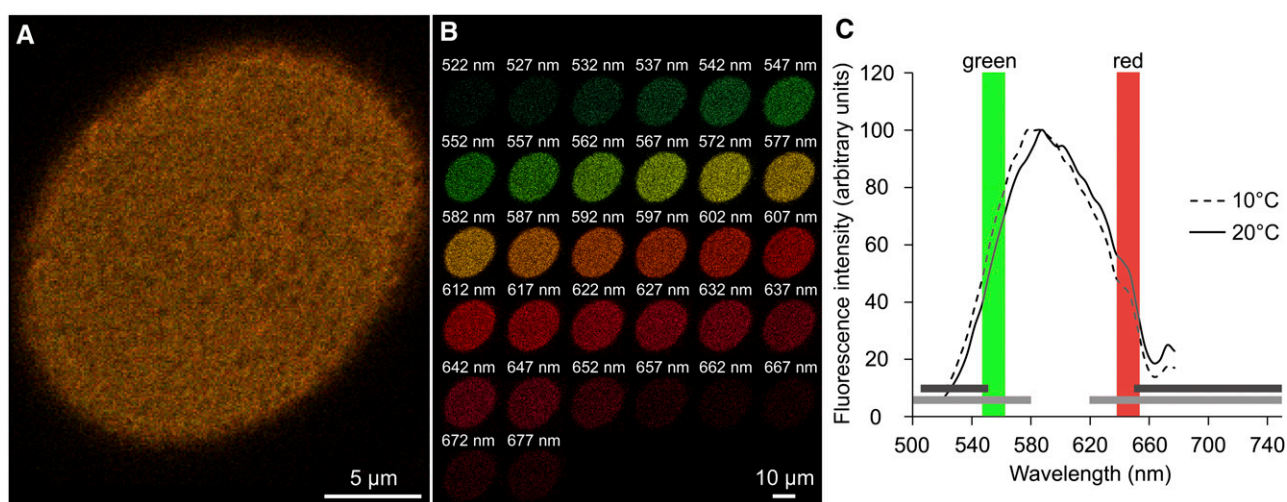

Figure 1. Characterization of the red/green ratio of a single-cell PM labeled with di-4-ANEPPDHQ by multispectral confocal microscopy. A, Observation of maximum surface area of di-4-ANEPPDHQ-labeled tobacco BY2 suspension cells (excitation at 488 nm; emission corresponds to the sum of fluorescence intensities acquired from all channels, ranging from 520 to 680 nm) with a color rendering of pixel fluorescence. B, Separate images for each wavelength corresponding to the emission fluorescence of a single channel captured by a 5-nm band pass (central value is reported). C, Representative emission spectra of di-4-ANEPPDHQ in tobacco cell PM exposed for 5 min at different temperatures ($n = 10$ independent cells for each condition). Depending on the device available, previous studies have used different band passes centered around 550 and 660 nm to quantify the blue shift of the dye on living material. For example, the horizontal, light gray bands correspond to 500 to 580 nm and 620 to 750 nm (Miguel et al., 2011), while the horizontal, dark gray bands correspond to 505 to 550 nm and a long pass higher than 650 nm (Liu et al., 2009). The colored, vertical band pass bars correspond to the values used in our experimental setup to calculate an accurate red/green ratio (545–565 nm in red and 635–655 nm in green).

noted for different biological materials (Dinic et al., 2011). The resulting lower red/green ratio is associated with an increase in the global level of membrane order (Supplemental Fig. S3). Emission spectra of di-4-ANEPPDHQ-labeled tobacco suspension cells exposed for 5 min to different temperatures likewise indicated a similar cold temperature-induced blue shift measured either by confocal multispectral setup (Fig. 1C) or classical spectrofluorimetry (Supplemental Fig. S4A). Moreover, the emission spectrum fluctuates with temperature in a comparable manner when PM fractions purified from tobacco suspension cells were used (Supplemental Fig. S4B), in line with previously published data (Roche et al., 2008).

Together, these results confirm that the combination of di-4-ANEPPDHQ labeling of tobacco suspension cells and multispectral confocal microscopy is suitable to monitor changes in the order level of living plant cell PMs.

Transient Modifications of PM Biophysical Properties Occur upon Elicitation

We analyzed the evolution of tobacco cell PM order level in response to 50 nM of cryptogein, an elicitor of defense reaction. Successive observations of single cells, performed within the first minutes of treatment, suggest a transient RGM decrease in cryptogein-elicited cells, but not in control cells (Supplemental Fig. S5). A statistical analysis of the fluorescence from many cells at different times after treatment confirmed a significant decrease in RGM (from 0.94 ± 0.02 to 0.84 ± 0.01) after 5 min of cryptogein elicitation (Fig. 2A). No significant difference was observed between control and elicited cells after 15 min of elicitation (Fig. 2A), indicating that the cryptogein-induced global increase in order level is transient. This was subsequently confirmed by monitoring cells with classical spectrofluorimetry (Supplemental Fig. S6). When cells were incubated 5 min with bovine serum albumin (BSA; 50 nM) or lysozyme (100 nM), a small globular protein that presents similar structural properties as cryptogein (13 kD, versus 10 kD for cryptogein and a basic internal pH of 11 versus 9 for cryptogein), no change in tobacco PM order level was observed by either spectral confocal microscopy (Fig. 2B) or spectrofluorimetry (Supplemental Fig. S7), ruling out the possibility that the decrease observed with cryptogein could correspond to a nonspecific effect.

To confirm the link between triggering of defense signaling and RGM modification, we used flg22, a known activator of plant defense mechanisms (Denoux et al., 2008), especially in tobacco cells (Lecourieux et al., 2002). The timing and intensity of the reactive oxygen species (ROS) productions triggered by flg22 (20 nM) and by cryptogein were comparable (Supplemental Fig. S8). After 5 min of treatment, a significant RGM decrease was detected in flg22-elicited cells compared with the control (Fig. 2B; Supplemental Fig. S7), confirming the link between the increase in PM order level and the elicitation process.

Along with order level, membrane fluidity is another feature that characterizes PM organization. We
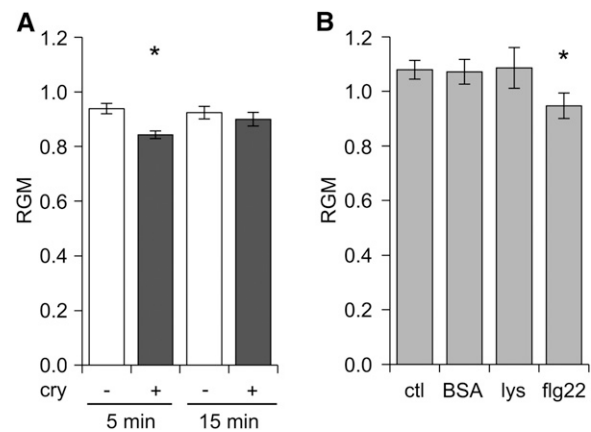

Figure 2. Increase of the global level of order at the PM surface of elicited tobacco cells. A, The time course of the RGM was followed after elicitation with 50 nM cryptogein (cry). B, The RGM was measured after 5 min treatment with 50 nM BSA, 100 nM lysozyme (lys), and 20 nM of flagellin (flg22) and compared to control cells (ctl). Data shown are mean values $\pm$ SE of the mean ($n = 14$–66 cells). The asterisk indicates a significant difference (P value < 0.05).

examined the effects of cryptogein on this second parameter through the diffusional mobility of di-4-ANEPPDHQ in the PM of Bright Yellow 2 (BY2)-elicited cells during FRAP experiments. This dye is effective for FRAP experiments, as its insertion is in alignment with the surrounding lipid molecules in the bilayer membrane. After labeling of tobacco cells, the PM was photobleached and dye mobility was monitored by the recovery of fluorescence (emission band pass, 510–700 nm; Fig. 3), as previously described (Bonneau et al., 2010). Cryptogein-elicited cells transiently exhibited faster fluorescence recovery kinetics than control cells (Fig. 3, A and B). After 5 min of cryptogein elicitation, the half time of fluorescence recovery was 31.6 ± 1.4 s ($n = 58$) and 25.4 ± 0.8 s ($n = 89$) for control and elicited cells, respectively (Fig. 3B); both cell conditions were associated with the same mobile fraction (Supplemental Fig. S9). No significant difference was observed between control and elicited cells after 15 min of cryptogein elicitation, and cells from each condition displayed a half time of fluorescence recovery of 34 s (Fig. 3B), indicating that the cryptogein-induced global increase in dye mobility is transient. Conversely, after 5 min of incubation, flg22, BSA, and lysozyme were all unable to induce a significant modification to the lateral fluidity of tobacco cells PM (Fig. 3C). This illustrates the specificity of the cryptogein-induced increase in diffusional mobility, as determined by di-4-ANEPPDHQ.

Spatial Organization of the Tobacco Cell PM Order Level

To investigate a possible lateral compartmentalization of the tobacco cell PM, we analyzed the di-4-ANEPPDHQ emission spectrum acquired as described above (compare with Fig. 1) within small regions of
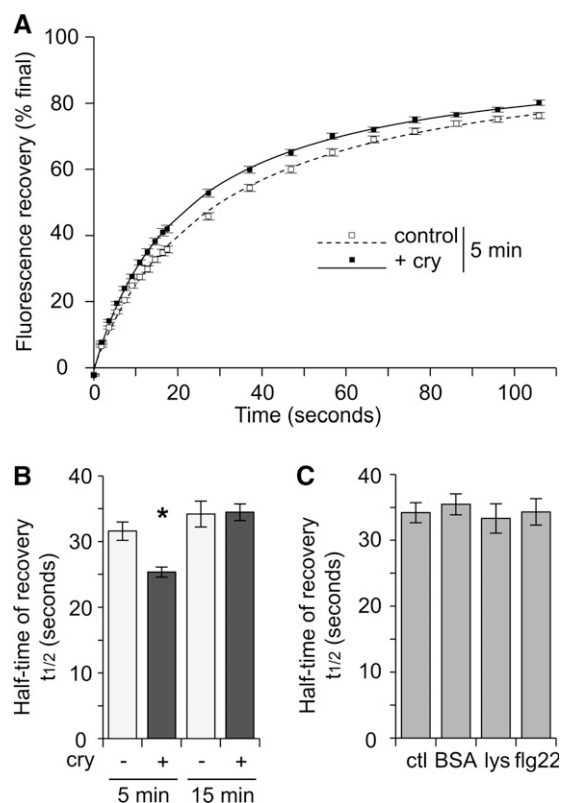
Figure 3. Influence of cryptogein treatment on the global fluidity of tobacco cell PM measured by FRAP. A, Normalized fluorescence recovery (excitation: 488 nm, emission: 510–700 nm) was plotted for control cells or cells elicited with 50 nM cryptogein (+cry) after 5 min of treatment. The fluorescence level is not normalized to the initial fluorescence, and only the mobile fraction is represented (final percentage: 100%). The plotted control and cryptogein lines represent results of fit to $F(t) = (F_0 + F\infty \times [t/t_{1/2}])/(1 + [t/t_{1/2}])$, where F_0 is the immediate postbleach intensity, $F\infty$ is the asymptote of fluorescence recovery, and $t_{1/2}$ is the time required to recover 50% of the asymptote fluorescence (error bars indicate ± SE of the mean). B, Influence of cryptogein elicitation treatment (cry) on half-maximal recovery. The asterisk denotes a statistically significant difference (P value < 0.01), and the data shown are mean values ± SE of the mean. For control cells, $n = 58$ (5 min) and 40 (15 min); for treated cells, $n = 89$ (5 min) and 52 (15 min). C, Influence of the treatments 50 nM BSA ($n = 25$), 100 nN lysozyme (lys; $n = 36$), and 20 nM flagellin (flg22; $n = 28$) on half-maximal recovery, compared with a control (ctl; $n = 48$). The asterisk denotes a statistically significant difference (P value < 0.01), and the data shown are mean values ± SE of the mean.

interest (ROIs, 288 nm × 288 nm). Comparing RGMs from the fluorescence of the whole cell surface and the average of the red/green ratios of each ROI comprising this surface (referred to as red/green ratio of the ROI [RGR]; Supplemental Fig. S3) yielded identical values (Fig. 4A). We used a stringent methodology previously described in the literature for noise removal from fluorescent images (Owen et al., 2012a). This analysis eliminates ROIs that exhibit a fluorescence intensity less than 7% of the highest intensity exhibited by a ROI within the analyzed membrane surface. No ROIs were eliminated, which indicates that ROIs retain enough fluorescent

intensity for further analyses, despite their small size. Furthermore, we explored a possible link between fluorescence intensity exhibited by a ROI and the corresponding RGR measurement. This was assayed by comparing the distribution of RGR values of a single cell to the distribution of either ROIs with the 10% highest fluorescence intensity or ROIs exhibiting fluorescence intensity over 80% of the maximum fluorescence intensity measured. In parallel, we randomly selected a sample of equivalent size from this latter sample. Neither the recorded fluorescence intensity of the ROI nor ROI arbitrary sampling was observed to influence the distribution of RGR values (Fig. 4B). As this distribution was identical across the different samples, this parameter does not appear to depend on ROI fluorescence intensity.

The analysis of RGR distribution revealed a highly reproducible, continuous distribution with a broad range of RGR values (from 0.3 to 2.5), indicating the presence of order level heterogeneity within the different ROIs present on a PM surface. This distribution is centered on 0.9 and shows that 75% of ROIs have a RGR value between 0.6 and 1.2 (Fig. 5A).

To investigate the influence of PM sterol amount on this heterogeneity, we used methyl-β-cyclodextrin (MβCD), a sterol-depleting molecule that decreases the order level of both purified biological membranes (Roche et al., 2008) and living cell membranes (Kucherak et al., 2010). Treatment of tobacco cells with 5 mM MβCD led to a 21% ± 7% reduction (SD, $n =$ nine independent experiments) in the PM sterol amount after 20 min of treatment. The RGM of MβCD-treated cells labeled with di-4-ANEPPDHQ was significantly increased (1.3-fold) compared with control cells, indicating a decrease in the level of tobacco PM order after
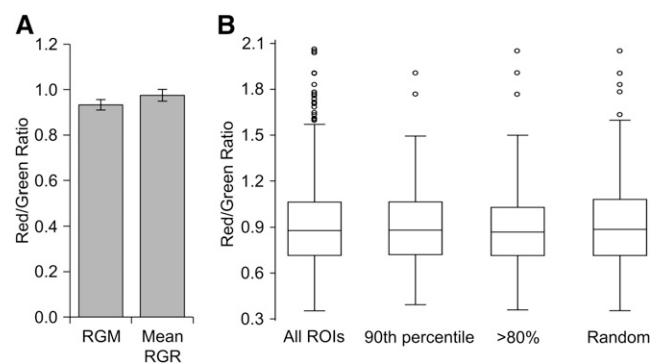

Figure 4. Analysis of different levels of order within the PM of tobacco cells. A, Comparison of PM order level, using RGM (the red/green ratio calculated from the global emission spectrum exhibited by the entirety of imaged cell membrane areas) or mean RGR (the average of the ratios of individual ROI [288 nm × 288 nm] of the cell surface area; mean ± SE of the mean, $n = 49$ cells). B, Comparison of RGR distribution from a single cell (all ROIs) with RGR distributions corresponding to the 10% of ROIs exhibiting highest fluorescence intensity (over the 90th percentile value); ROIs exhibiting fluorescence intensity above 80% of the maximum fluorescence intensity measured (>80%); and randomly selected ROIs from the same range as the greater than 80% sample (Random).

sterol depletion (Fig. 5B). The distribution of RGRs was still continuous but consistently shifted to higher values (Fig. 5A). Centered on 1.2, the distribution of MβCD-treated cells is flattened compared with the control distribution, indicating that 75% of ROIs have an RGR value between 0.8 and 1.7 (Fig. 5A). These data were analyzed by thresholding RGRs at different values. Based on previous results from purified tobacco PM fractions (Roche et al., 2008), 0.6 represents a threshold below which the isolated PM is in Lo phase in our system. The remaining threshold values include 0.8 (the lowest quartile of RGR distribution; Fig. 5A), 1.0 (close to the median value of the distribution of control cells; Fig. 5A), and 1.2 (maximum RGR distribution of MβCD-treated cells; Fig. 5A). Regardless of whichever upper RGR threshold value was used to select ROIs corresponding to the most ordered fraction of the membrane, MβCD induced a significant decrease in the relative proportion of these regions, which was more pronounced when the threshold was low (Fig. 5C).

These results indicate that RGR is directly related to the level of discretely measured membrane order. Furthermore, the distribution of these values suggests a lateral heterogeneity of the tobacco PM with respect to this parameter.

Cryptogein Induces a Spatial Rearrangement of the PM Order Level in Tobacco Cells

To investigate cryptogein-induced modifications in lateral compartmentalization of the tobacco cell PM according to its order level, we compared the RGR distribution of control and cryptogein-treated cells. When RGRs were pseudocolor coded with the highest values in green and the lowest values in red, the tobacco cell PM appeared as a heterogeneous mosaic of zones with different order levels (Fig. 6A). In addition, a greater coverage of red colors was observed in elicited cells

compared with the control (Fig. 6, A and B). Analysis of the distribution of RGRs consistently showed a shift to lower values after 5 min of cryptogein treatment (Fig. 6C). The shift was further quantified using two methods. The proportion of ROIs corresponding to the most ordered fraction of the membrane was calculated, and a significant increase was observed after cryptogein treatment, regardless of the chosen RGR threshold value (from 0.6 to 1.2; Table I). Interestingly, the increase in the lowest RGR values was more pronounced at lower thresholds, i.e. the 74% increase measured at the 0.6 upper limit decreased to 37% at the 0.8 threshold, pointing out the crucial involvement of lowest RGR values in the cryptogein-induced shift of RGR distribution (Table I). No difference was measured between control- and lysozyme-treated cells (Supplemental Fig. S10), whereas flg22 treatment significantly increased the proportion of ROIs exhibiting the lowest RGR (Supplemental Fig. S10). This suggests that ROIs that exhibit the lowest RGRs are predominantly involved in the elicitor-induced decrease of PM order level.

An adaptive threshold that keeps the amount of considered ROIs constant could also be a relevant estimate of RGR distribution. Consistent with the results described above, cryptogein elicitation significantly decreased the mean RGR of the first quartile (i.e. 25% of ROIs with the lowest RGR values) from 0.76 ± 0.13 in control cells to 0.64 ± 0.07 in elicited cells, confirming the cryptogein-induced increase of ROI order level.

A routine granulometric approach revealed that cryptogein treatment, previously shown to increase the total amount of ROIs with a RGR below 0.8 (Table I), both decreased the proportion of isolated ROIs and increased the fraction of ROIs lying within clusters (Supplemental Fig. S11A). Concomitantly, the mean size of groups of these ROIs increased in elicited cells (Supplemental Fig. S11B). To avoid density effects, we performed such analysis by keeping the number of
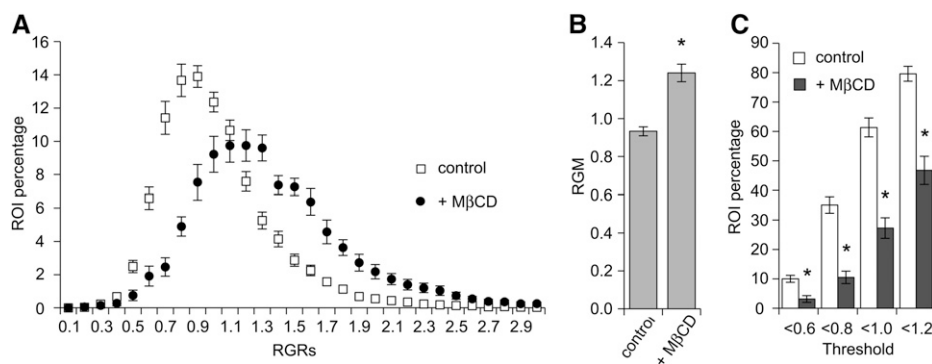

Figure 5. Heterogeneity of the order level of tobacco cell PM is sterol sensitive. A, Distribution of red/green ratio values of individual ROIs (288 nm × 288 nm) of the PM and influence of sterol depletion (+MβCD). The x axis corresponds to the class of RGR values, and only the maximal value of each class is reported on the graph. The y axis corresponds to the ROI percentage of each class. B, Influence of sterol depletion (+MβCD) on RGM. C, Representativeness of low RGR values according to PM sterol content. ROIs exhibiting an RGR below the threshold values indicated on the x axis were counted, and their percentage was reported along the y axis for control (white) and treated (black) cells. For both B and C, asterisks indicate a significant difference (P value < 0.01), and data are means ± SE of the mean (n = 49 [control] and 11 [treated cells]).
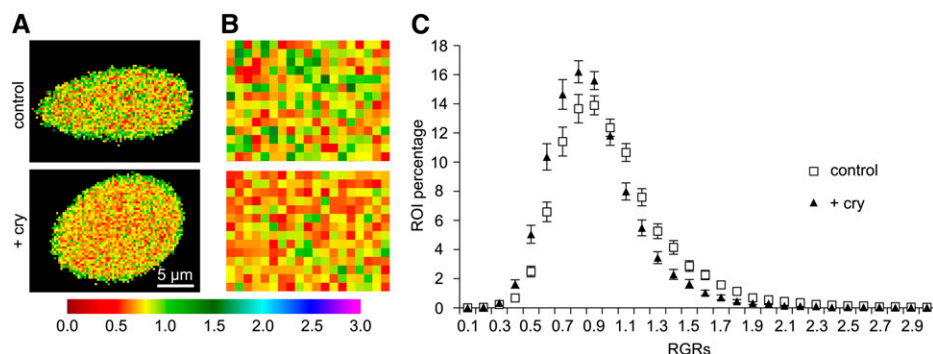
Figure 6. Increase of the proportion of ROIs with low RGR at the PM surface of cryptogein-elicited tobacco cells. Ratiometric images of tobacco BY2 suspension cells that were either elicited with cryptogein (bottom) or not (top) are displayed in A and B. A, A pseudocolor-coded representation of total cell surface area, according to the accompanying RGR scale. B, Zoom of an area extracted from the plant membrane surface (ROI size: 288 nm × 288 nm). C, Comparison of RGR distribution between cryptogein-treated (black triangles) and control cells (white squares). The x axis represents the class of RGRs values; only the maximal value of each class is reported on the graph. The y axis represents the percentage of each class of ROI values. Data are means ± SE of the mean (n = 49 cells for both conditions).

ROIs in control and treated samples constant by considering only the first quartile of lower RGR values (Supplemental Fig. S11C). No change in the mean size of these ROI groups was then observed after cryptogein treatment (Supplemental Fig. S11D). We conclude that cryptogein induced an apparent aggregation of low RGR ROIs (Supplemental Fig. S11A), exclusively by increasing their density.

DISCUSSION

Multispectral Confocal Microscopy Reveals a Lateral Heterogeneity in the Tobacco Plasma Membrane

Numerous biophysics reports have used giant unilamellar vesicles prepared with different lipid mixtures to propose that model membranes can exhibit a lateral phase coexistence of gel/fluid phases (Wesołowska et al., 2009). Depending on the lipid mixture, Lo, Ld, and even gel phase separation can occur. Optically resolvable Lo/Ld phase domains in lipid model membranes were initially studied through fluorescence microscopy by examining the partitioning of fluorescent lipids between the gel and Ld phases (Klausner and Wolf, 1980). More recently, environmentally sensitive probes have been used to clearly establish the coexistence of Lo and Ld phases in model membrane systems (Klymchenko et al., 2009). Similar type of phase separation has also been observed in biological systems, e.g. by imaging the diffusion coefficient of fluorescent lipid analogs in primary oligodendrocytes (Gielen et al., 2009). However, fluorescence ratiometric images of human glioblastoma cells labeled with di-4-ANEPPDHQ show a remarkable homogeneity in the distribution of the Lo/Ld phases, which is likely due to the limited spatial and temporal resolution of optical microscopy (Oncul et al., 2010).

Here, we have described the heterogeneity of tobacco PM lateral organization with respect to its order

level by measuring the red/green ratio of the environmentally sensitive probe di-4-ANEPPDHQ within small ROIs. We obtained an RGR distribution that was independent of the fluorescence intensity of each ROI (Fig. 4), which affirms the robustness of this parameter in evaluating the order level of the analyzed zone. The degree of cell membrane order evaluated from the emission properties of the dye can also be expressed as a generalized polarization parameter (GP), defined as (I550 − I660)/(I550 + I660), which increases with ordered level (Owen et al., 2010b, 2012a; Miguel et al., 2011). Interestingly, the fact that tobacco cell PM can be observed as a continuous distribution centered on a unique peak by using either the GP (Supplemental Fig. S10) or RGR (Fig. 6) fluorescent parameters is not indicative of the coexistence of only two major different phases (Lo/Ld).

A similar heterogeneity of local order level has been observed at the PM of animal cells, revealing a common GP continuous distribution, although various ranges of membrane order values were exhibited, depending on the technique and the probe used (Gaus et al., 2006; Wheeler and Tyler, 2011). For example, relatively close GP values have been measured in HeLa cells (from −0.2

Table I. *Proportion of ROI exhibiting lowest RGR values in control and cryptogein-treated cells*

ROIs exhibiting an RGR ratio below the upper threshold (corresponding to the first column) were counted, and their percentage of the total ROI was measured in control and cryptogein treated-cells (cry). The cryptogein-induced increase in the amount of ROI exhibiting low RGR was reported as a percentage of the control amount. Data are means of 49 cells for all conditions; the P value is reported.

Upper Threshold	ROI Percentage		Increase Percentage	P Value
<0.6	10.0	17.4	74.0	0.001
<0.8	35.1	48.3	37.6	0.001
<1.0	61.4	75.7	23.3	0.001
<1.2	79.6	89.2	12.1	0.002

to 0.4) labeled with di-4-ANEPPDHQ (Owen et al., 2012b), whereas a larger distribution of GP values in laurdan-labeled cells has been described for epithelial cells of the zebrafish gut (from –1 to 1; Owen et al., 2010b). Consistent with these studies, we observed a symmetric distribution of GP values in tobacco cells, from –0.4 to 0.6 (Supplemental Fig. S12). These values are in agreement with those observed from the PM of Arabidopsis protoplasts, where GP ranged from –0.3 to 0.2 immediately after enzymatic digestion of the cell wall, up to a value of 0.6 15 h later (Blachutzik et al., 2012).

A similar broad histogram distribution was previously described using fluorescence lifetime imaging in live epithelial cells labeled with di-4-ANEPPDHQ (Owen et al., 2006), as well as laurdan-labeled K562 cells (Balogh et al., 2011). Combined fluorescence anisotropy and polarization-resolved fluorescence imaging revealed a similar histogram distribution in di-8-ANEPPQ orientational order measured in COS7 cells (Kress et al., 2011). Fluorescence correlation spectroscopy, well suited to explore the spatial organization pattern of fluidity, allowed the description of a continuous broad distribution of the diffusion time in 4-(4-(dihexadecylamino)styryl)-N-methylpyridinium iodide (DiA)-labeled MFC7 cells (Winckler et al., 2012) and of the diffusion coefficient in HeLa cells (Gerken et al., 2012). Atomic force microscopy has been exploited to spatially map the pulmonary endothelial monolayer and to define the continuous distribution of cell stiffness, as revealed by a broad histogram distribution of its elastic modulus (Birukova et al., 2009). The similarity in histogram distribution shapes observed with these different techniques strongly supports a view in which parameters that reflect order heterogeneity within biological membranes show a broad range of values. Moreover, two-photon images of the effect of MβCD treatment and temperature changes on laurdan fluorescence show that cholesterol shifted to lower values and narrowed the distribution of GP values; this demonstrates that membrane order depends on temperature and cholesterol in different models (Heiner et al., 2008; Wheeler and Tyler, 2011). In our study, a similar influence of sterol amount on the global red/green ratio of di-4-ANEPPDHQ and on the proportion of ROI exhibiting low RGR was observed in tobacco cell PM (Fig. 5). This observation, associated with the distribution shift in response to cryptogein (Fig. 6), argues in favor of a biological reality underlying the observed heterogeneity of RGR values.

This heterogeneity of membrane order level might occur at the nanoscale range, because the surface of analyzed ROIs corresponds to a 288-nm-edge square. Such a nanoscale lateral heterogeneity has already been reported for several membrane components. For instance, tagged protein clusters have been observed at this scale on several substrates, including cardiac myocytes (Ianoul et al., 2005), HeLa cells (Abulrob et al., 2008), and PM sheets (Parton and Hancock, 2004). Multidistance spatial cluster statistics analysis (Ripley's *k* function) of the immunogold-labeled ganglioside GM1

showed spatial aggregation in normal mouse fibroblasts for distances ranging from 32 to 68 nm (Fujita et al., 2007). Similarly, plant-based immunoelectron microscopy experiments have revealed partitioning of both the lipid phosphatidylinositol 4,5-bisphosphate into 25-nm clusters on the PM of tobacco BY2 cells (Furt et al., 2010) and the protein flotillin into clusters of less than 100 nm on the PM of Arabidopsis roots apices (Li et al., 2012). In addition, the protein remorin was observed by immunoelectron microscopy in domains of about 80 nm in the cytosolic leaflet of the membrane of tobacco leaves (Raffaele et al., 2009) and was more recently localized by stimulated emission depletion microscopy within domains of 97 nm in Arabidopsis, whereas the apparent size of these domains was about 250 nm, using classical confocal microscopy (Demir et al., 2013). Similarly, the heterogeneity of RGR values that we observed could correspond to domains of 100 nm or less. Consistent with these observations, single particle tracking experiments performed on Arabidopsis roots to study the dynamics of the PM intrinsic protein PIP2;1 have revealed that about 20% of PIP2;1 fused to GFP exhibited a confined diffusion, with an average confinement range of about 90 nm (Li et al., 2012).

Thus, our study of the lateral distribution of an environmentally sensitive probe's fluorescent parameters on the PM of tobacco suspension cells suggests a heterogeneity of the PM level order at a nanoscale range. These observations are in agreement with the lateral segregation of membrane components that have been previously illustrated with various techniques.

Cryptogein Transiently Induces a Modification in Tobacco Cell PM Heterogeneity Together with an Increase in Membrane Fluidity

We observed within minutes of adding cryptogein to tobacco suspension cells an increase in the relative amounts of those ROIs that exhibit the lowest RGR (corresponding to the most ordered fraction of the membrane). This result is in agreement with an established ordered domain enrichment at specific cell regions, e.g. at the site of T lymphocyte activation (Gaus et al., 2005). Single living human acute monocytic leukemia cell line macrophages have also been observed to exhibit an increase in the amount of ordered domains, when oxidized with hydrogen peroxide (de la Haba et al., 2012).

A role for dynamic PM compartmentalization in response to environmental signals has recently begun to emerge in plant cells (Zappel and Panstruga, 2008; Mongrand et al., 2010; Simon-Plas et al., 2011), following a concept previously proposed in animal cells (Simons and Sampaio, 2011). Recent studies have shown how several abscisic acid signaling components interact within nanodomains in response to this phytohormone (Demir et al., 2013), as well as how the *S*-acylation of the small G protein Rop6 (which conditions its dynamic association to DIMs) is a critical determinant of its role in the regulation of cell polarity (Sorek et al., 2011). In our system, the PM-localized

NADPH oxidase that is responsible for ROS production upon cryptogein treatment was previously revealed to associate exclusively with the DIM fraction; furthermore, its product is localized within 100-nm patches along the membrane within minutes of elicitation (Lherminier et al., 2009). Moreover, an association of specific proteins with DIMs (including a 14-3-3 protein that is a positive regulator of cryptogein) has been observed within minutes of treating tobacco cells with cryptogein (Elmayan et al., 2007; Stanislas et al., 2009). Similar results have been reported in the Arabidopsis-flagellin model: changes in the protein composition of DIMs extracted from cultured cells were triggered within 5 min by the addition of flg22, including an enrichment of the receptor-like kinase *Arabidopsis thaliana* Flagellin Sensing2 (Keinath et al., 2010). These findings point to a role for sterol-enriched ordered domains in the regulation of the signal transduction associated with plant defense and are in agreement with the coalescence of sterol-rich domains in barley (*Hordeum vulgare*) in response to the penetration of *Blumeria graminis* (Bhat et al., 2005). We have demonstrated here that flg22, which triggers signaling events in BY2 cells (Supplemental Fig. S8), induces a decrease in RGM (similar to cryptogein), whereas biologically inactive control proteins did not. This result strongly suggests that such a prompt modification of the PM order level might be a general process associated with the onset of plant defense signaling.

Cryptogein induces in tobacco cells a quick and transient increase in membrane fluidity. Such alterations in membrane fluidity are among the first responses in plants facing changes in ambient temperature whose events include a heat-signaling pathway (Königshofer et al., 2008), a cold perception mechanism (Vaultier et al., 2006), and a chilling stress response (Alonso et al., 1997). In our model, an identical magnitude in variation (10%–15%) observed for both the proportion of ordered phase and the membrane fluidity, together with similar transient kinetics observed for these two events, argues in favor of the existence of a functional link between these two cryptogein-induced modifications to PM characteristics. Observations that associate membrane fluidity variations with proportion of ordered phase have previously been reported in a model membrane (M'Baye et al., 2008). A higher fluidity has been associated with a more stable concentration of ordered domain markers in discrete spots at the leukemia T cell membrane in response to a mechanical stimulus; this suggests a tight interplay between rheological membrane properties and cytoskeleton components (Verstraeten et al., 2010). Similarly, temperature- and benzyl alcohol-induced fluidification were shown to be associated with an increase in large, cholesterol-rich domains in melanoma cells (Nagy et al., 2007). Ethanol-induced oxidative stress is dependent on the clustering of lipid ordered domains in primary rat hepatocytes (Nourissat et al., 2008) and is associated with membrane fluidity increase (Sergent et al., 2005). The transient fluidification of the tobacco cell PM specifically induced by cryptogein (Fig. 3) could thus favor membrane reorganization through processes such as

lateral moving and/or membrane fusion. In particular, the inducible targeting at the PM surface of Golgi vesicles enriched in Lo domains (Laloi et al., 2007) could increase the representativeness of ordered domains at the cell surface (Fig. 6). A role for the endocytic pathway in DIM-enriched protein localization at specific sites in root cells and seedlings was accordingly demonstrated for aquaporin (Luu et al., 2012), dynamin-related protein (Konopka et al., 2008), and flotillin (Li et al., 2012).

In contrast to the increase in RGM observed in response to both cryptogein and flagellin treatment, the transient increase in fluidity observed with elicitin did not occur upon treatment of BY2 cells with flg22 (Fig. 3). This result suggests that the reduction in diffusional mobility of the FLS2 receptor induced by flagellin activation (Ali et al., 2007) might be limited to this receptor and its possible interactors. This result highlights the complexity and specificity of the signaling cascades activated by the commonly named elicitors of defense reactions. If considerable overlap has been found in the responses to different elicitors, suggesting that they activate conserved basal defense responses (Jones and Dangl, 2006), the particular suite of early signaling events, or associated kinetics and intensity, varies depending on the specific elicitor (Garcia-Brugger et al., 2006). Cryptogein and flagellin trigger common signaling events such as ROS production, medium alkalinization, MAP kinase activation, calcium influx, endocytosis, or induction of gene expression (Gómez-Gómez et al., 2002; Garcia-Brugger et al., 2006; Chinchilla et al., 2007; Denoux et al., 2008; Leborgne-Castel et al., 2008), although some discrepancies exist between these two proteinaceous elicitors. For instance, both elicitors induce changes in nuclear and cytosolic Ca^{2+} concentrations, yet the changes vary in magnitude and timing (Lecourieux et al., 2005). Whereas cryptogein induces a well-characterized HR in tobacco plants and cell death in suspension cells, flagellin acts as a nonnecrotic elicitor (Denoux et al., 2008). Moreover, cryptogein induces a dramatic depolymerization of cortical microtubules in tobacco cells after 1 h of treatment (Binet et al., 2001), whereas flg22 did not cause any such changes in the radial or cortical microtubules (Guan et al., 2013). If the modification of the global level of PM order could be part of the conserved basal defense responses, the transient modification of membrane fluidity might correspond to a more specific response. More detailed investigations are necessary to determine which other common or distinct steps of the global defense process these two new signaling cascade elements are related to.

Spatial Distribution and Dynamic of PM Heterogeneity

Raster image correlation spectroscopy is a valuable tool for precisely mapping the cell membrane organization and has been put to successful use in measuring molecular dynamics (Gielen et al., 2009). However, this method yields a high proportion of pixels that only contain background signal, thus preventing an

accurate spatial analysis (Gielen et al., 2009). To avoid this scenario, we have used a confocal microscopy setup with a whole surface acquisition and sufficient sensitivity to describe plant membrane biophysical properties (Fig. 4). This surface cover ability is compatible with the spatial characterization of ordered domains.

Our results suggest a cryptogein-induced modification in the lateral organization of ordered domains, in particular the appearance of larger ordered domains (Supplemental Fig. S11). This result is in agreement with the prior use of an environmentally sensitive probe that established the enlargement of ordered domain size in T lymphocytes (Gaus et al., 2005). Moreover, the lateral distribution of fluorescently linked lipidic DIM markers was reorganized from nanometer- to micrometer-sized phases enriched in GM1, after cross linking by cholera toxin B (Lingwood et al., 2008). Combined, these reports have promoted a model of the stress-induced production of a signaling platform composed of coalesced lipid domains (Lingwood and Simons, 2010; Simons and Sampaio, 2011), which suggests the enhancement of ordered domain sizes. The results of the granulometic approach performed here are in line with this model and indicate that the cryptogein-induced larger size of Lo areas was mostly due to the increased proportion of ROIs exhibiting low RGRs. This might involves the targeting (via cell trafficking) of ordered domains at the PM. This hypothesis must now be confirmed with super resolution techniques that permit a direct characterization of the nanoscale dynamic domains occurring at the cell membrane.

Could the Membrane Raft Hypothesis Account for the Observed PM Nanoscale Heterogeneity?

In this model, lipid rafts are proposed to correspond to dynamic, Lo nanodomains enriched in sterols and sphingolipids that are able to coalesce into larger structures after stress induction; this type of dynamic lateral segregation is essential for many key physiological processes, including response to pathogens (Lingwood and Simons, 2010; Simons and Sampaio, 2011). Although this "raft hypothesis" is still under debate, several lines of experimental evidence strongly support the existence and dynamics of such domains. This includes the nanoscale lateral heterogeneity of membrane components, such as proteins or lipids, and the sensitivity of the lateral distribution of the membrane to sterol amount (Vereb et al., 2000; Raffaele et al., 2009), which points to a sterol-driven formation of nanodomains. The results presented here are in agreement with a nanoscale heterogeneity of the plant PM and the presence on the membrane of very small areas (less than 300 nm) of various levels of order. This fits with the lipid organization defined at the nanometer scale by atomic force microscopy using ternary lipid mixture vesicles (Rinia and de Kruijff, 2001; El Kirat et al., 2010; Giocondi et al., 2010). Furthermore, the sterol dependency of this or ganization, demonstrated in this work by the cyclodextrin-induced modification of RGR distribution

(Fig. 2), is in agreement with previous data. The depletion of membrane sterols induced by MβCD was observed to result in a disruption to the clustered organization of the protein remorin (Raffaele et al., 2009), indicating the sterol-dependent confinement of this protein into domains of 100 nm. Accordingly, both the clustering in domains of remorin and PIP2;1 were dramatically affected by treatment with cyclodextrin (Raffaele et al., 2009; Li et al., 2012), indicating a major role for sterols in the spatial segregation of these proteins in membrane domains. This treatment also induced an overall increase in acyl chain disorder and a reduction in liquid phase heterogeneity of isolated tobacco PM (Roche et al., 2008), in line with the ability of phytosterols to induce a Lo phase in ternary mixtures of lipids (Beck et al., 2007). Here, we contribute new evidence in support of the developing "membrane raft" concept by revealing a large-range distribution of the sterol-dependent ordered level of nanoscale assemblies in plant suspension cells.

The raft hypothesis postulates that, in response to external signals or the initiation of membrane trafficking events, raft platforms ranging in size from 20 to 200 nm are formed from nanoscale domains through lipid-lipid, lipid-protein, and protein-protein oligomerizing interactions (Simons and Gerl, 2010). Our study postulates an original mean to produce signaling platforms, by enrichment at the membrane surface of small-size ordered domains and provides evidence for this process during the very early steps of defense signal transduction.

In summary, we used a multispectral confocal microscopy setup to characterize the sterol-dependent heterogeneity of tobacco cell PM organization. These results suggest the coexistence of areas exhibiting different levels of order, which must next be examined by high-resolution methodologies. We have revealed a modification of both global and local membrane physical properties during the early steps of the cryptogein-induced signaling process, in particular an increase in ordered domains density. These results expand our view of the function of biological membranes, while remaining within the scope of the membrane raft hypothesis. Future research will examine the underlying cellular mechanisms of this dynamic organization, which will be complemented by elucidating their precise role in the signal transduction process.

MATERIALS AND METHODS

Materials

Tobacco (*Nicotiana tabacum*) BY2 cells were grown in Murashige and Skoog modified medium at pH 5.6 containing Murashige and Skoog salt supplemented with 1 mg L^{-1} thiamine-HCl, 0.2 mg L^{-1} 2,4 dichlorophenylacetic acid, 100 mg L^{-1} myoinositol, 30 g L^{-1} Suc, 200 mg L^{-1} KH$_2$PO$_4$, and 2 g L^{-1} MES. Cells were maintained under continuous light conditions (200 μE m^{-2} s^{-1}) on a rotary shaker (140 rpm) and weakly diluted (2:80) into fresh medium.

Chemicals Treatments

Cells were harvested 7 d after subculture, filtered, and resuspended (1 g/10 mL) in an incubation medium (2 mM MES buffer, pH 5.9, containing 175 mM mannitol,

0.5 mM CaCl$_2$, and 0.5 mM K$_2$SO$_4$). After a 3-h equilibration period on a rotary shaker (140 rpm) at 25°C, cells were treated with chemicals as indicated in the figure legends. Di-4-ANEPPDHQ (1-[2-hydroxy-3-(N,N-dimethyl-N-hydroxyethyl) ammoniopropyl]-4-[b-[2-(di-n-butylamino)-6-napthyl] vinyl] pyridinium dibromide) was purchased from Molecular Probes. Cryptogein was purified according to a previously published method (Ricci et al., 1989), prepared in distilled water, and used at a final concentration of 50 nM. For sterol depletion, BY2 cells were incubated 15 min with 5 mM MβCD (cell culture tested, Sigma-Aldrich). Concentrated (1,000-fold) stock solutions in water of BSA (Sigma-Aldrich), lysozyme (from chicken egg white, Sigma-Aldrich), and flg22 (kindly provided by Stéphane Bourque; Lecourieux et al., 2005) were individually added to cell suspensions at a final concentration of either 50, 100, or 20 nM, respectively.

PM Purification

Highly enriched BY2 cell PM fractions were prepared from 100 g of liquid nitrogen frozen cells, according to Mongrand et al. (2004).

Gas Chromatography and Sterol Quantification

Total lipids were extracted using Bligh and Dyer's method (Roche et al., 2008). Briefly, 400-μg cells were filtered and frozen in liquid nitrogen, where they were maintained for 30 min. Cell pellets were transferred to glass tubes and resuspended in a solution of 2 mL methanol-chloroform (1:2, v/v), supplemented with epicoprostanol (5β-cholestan-3α-ol, 100 μL in methanol) as the internal recovery standard for quantification. After brief sonication, 1 mL NaCl 0.9% (v/v) was added and lipids were saponified by heating 1 h at 80°C with 1 mL ethanol and 100 μL KOH (11 N). The nonsaponifiable fraction containing total sterols was extracted by hexane and transformed into its trimethylsilyl derivatives. Analytical gas chromatography was performed with a Chrompack chromatograph, as previously adapted (Roche et al., 2008).

Fluorescence Spectroscopy

Fluorescence measurements were performed on a Fluorolog-3 FL3-211 spectrometer (Jobin-Yvon, Horiba) in the T-format with one double monochromator for excitation and two single monochromators for emission light. Detection was achieved by two photomultipliers. The light source was a xenon arc lamp. The spectrophotometer was equipped with movable excitation and emission polarizers. All fluorescence signals were recorded with emission and excitation bandwidths of 5 nm and systematically corrected from light scattering with an unlabeled sample. Integration time was 1 s for spectra- and temperature-dependent traces. All data were acquired with the Datamax software (Jobin-Yvon/Thermo Galactic). Samples were stirred and equilibrated in a temperature-controlled chamber using a thermoelectric Peltier junction (Wavelength Electronics). Experiments were performed using a 10-mm special optic glass path cuvette filled with 2 mL of equilibrated suspension cells.

FRAP Experiments

A Leica TCS SP2-AOBS laser scanning confocal upright microscope coupled to a 488-nm line of an argon laser was used for excitation with a detection bandwidth of 510 to 700 nm. Cells were observed using a Plan Apochromat 40× oil immersion objective (numerical aperture, 1.25), and the detection pinhole was set to the optimum value of 1 Airy unit. All experiments were performed according to previously published method (Bonneau et al., 2010). Briefly, 1 mL of BY2 cell suspension was labeled for 60 s with 2 μL 1.5 mM di-4-ANEPPDHQ stock solution (in dimethyl sulfoxide) and then washed in incubation medium before cryptogein addition for 5 or 15 min. Five prebleach scans (one scan every 800 ms) at 8% maximal laser power were used to determine initial fluorescence intensity, after which one photobleaching scan was executed at 100% laser power. Postbleach fluorescence recovery was then sampled at 8% laser power for 106 s. A second FRAP measurement was systematically performed on the same exact cell and bleach region.

Confocal Multispectral Microscopy

BY2 cell suspension (500 μL) was labeled for 60 s with 1 μL 1.5 mM di-4-ANEPPDHQ stock solution (in dimethyl sulfoxide), after which cryptogein (50 nM) was added. Subsequently, a drop of treated cells was placed between the slide and coverslip just before microscopy observation. All experiments

were performed at room temperature (21°C) in incubation medium. A Nikon C1Si/PicoQuant inverted microscope with a Nuance CRi spectral camera was used to observe cells. Images were acquired with a Plan Apochromat 100.0×/1.40/0.13 oil immersion objective. A dichroïc slide (405–488nm), which slightly modifies the emission spectrum in red wavelengths, was used to increase the fluorescent signal recovery. High spectral resolution was achieved through the use of a fine-ruled diffraction grating, allowing a 5-nm channel resolution. The dispersed light was captured simultaneously at different wavelengths using 32 independent channels of a photodetector multianode array (compare with Fig. 1A). Cells were observed by focusing on the maximum area of the cell membrane (compare with Supplemental Fig. S2), and acquisition was performed for a square surface (25-μm side length) at a 256-pixel resolution, according to the recommended sampling theorem (Nyquist) and resolution limit of the microscope.

Image Processing and Spatial Analysis

Recorded images were decomposed for each of the 32 emission channels (compare with Fig. 1A), and individual files were transferred to ImageJ software (http://rsbweb.nih.gov/ij/). Red (respectively green) intensities were then computed by averaging four intensities from 545 to 565 nm (respectively 635 to 655 nm). To limit the background values, we thresholded images before calculation; this eliminates dim pixels with a poor signal-to-noise ratio (Owen et al., 2012a). Background values were defined as intensities below 7% of the maximum intensity of the cell (Gaus et al., 2003; Abulrob et al., 2008). Homogeneous square regions were extracted from each image. Spatial analysis was performed on ROIs by summing the fluorescence intensities of 3 × 3 pixels (ROI size: 288 nm × 288 nm).

Statistical tests

Statistical inference was based on Student's t test.

Supplemental Data

The following materials are available in the online version of this article.

Supplemental Figure S1. Subcellular localization of di-4-ANEPPDHQ labeling of tobacco suspension cells.

Supplemental Figure S2. Large surface area observation of the tobacco cell PM.

Supplemental Figure S3. Schematic drawing explaining the principle of our measurements.

Supplemental Figure S4. Spectrofluorimetry monitoring of fluorescence variations according to temperature.

Supplemental Figure S5. Single cell kinetics of cryptogein-induced increase in PM order level.

Supplemental Figure S6. Spectrofluorimetry monitoring of the increase in PM order level induced by cryptogein elicitation.

Supplemental Figure S7. Spectrofluorimetry monitoring of PM order level modifications induced by elicitors.

Supplemental Figure S8. ROS production induced by cryptogein and flg22 in tobacco suspension cells.

Supplemental Figure S9. Influence of elicitation treatment on the mobile fraction during two consecutive bleach and rebleach sessions.

Supplemental Figure S10. Effect of lysozyme and flagellin treatments on RGR distribution.

Supplemental Figure S11. A granulometric approach reveals a tendency for pixels with low RGR values to spatially aggregate in elicited cells.

Supplemental Figure S12. General polarization analysis reveals an increase in the proportion of ROI exhibiting low order level at the PM surface of elicited tobacco cells.

LITERATURE CITED

Abulrob A, Lu Z, Brunette E, Pulla D, Stanimirovic D, Johnston LJ (2008) Near-field scanning optical microscopy detects nanoscale glycolipid domains in the plasma membrane. J Microsc **232:** 225–234

Ali GS, Prasad KV, Day I, Reddy AS (2007) Ligand-dependent reduction in the membrane mobility of FLAGELLIN SENSITIVE2, an Arabidopsis receptor-like kinase. Plant Cell Physiol **48:** 1601–1611

Alonso A, Queiroz CS, Magalhães AC (1997) Chilling stress leads to increased cell membrane rigidity in roots of coffee (*Coffea arabica* L.) seedlings. Biochim Biophys Acta **1323:** 75–84

Bagatolli LA (2006) To see or not to see: lateral organization of biological membranes and fluorescence microscopy. Biochim Biophys Acta **1758:** 1541–1556

Balogh G, Maulucci G, Gombos I, Horváth I, Török Z, Péter M, Fodor E, Páli T, Benko S, Parasassi T, et al (2011) Heat stress causes spatially-distinct membrane re-modelling in K562 leukemia cells. PLoS ONE **6:** e21182

Baumgart T, Hammond AT, Sengupta P, Hess ST, Holowka DA, Baird BA, Webb WW (2007) Large-scale fluid/fluid phase separation of proteins and lipids in giant plasma membrane vesicles. Proc Natl Acad Sci USA **104:** 3165–3170

Beck JG, Mathieu D, Loudet C, Buchoux S, Dufourc EJ (2007) Plant sterols in "rafts": a better way to regulate membrane thermal shocks. FASEB J **21:** 1714–1723

Bhat RA, Miklis M, Schmelzer E, Schulze-Lefert P, Panstruga R (2005) Recruitment and interaction dynamics of plant penetration resistance components in a plasma membrane microdomain. Proc Natl Acad Sci USA **102:** 3135–3140

Binet MN, Humbert C, Lecourieux D, Vantard M, Pugin A (2001) Disruption of microtubular cytoskeleton induced by cryptogein, an elicitor of hypersensitive response in tobacco cells. Plant Physiol **125:** 564–572

Birukova AA, Arce FT, Moldobaeva N, Dudek SM, Garcia JG, Lal R, Birukov KG (2009) Endothelial permeability is controlled by spatially defined cytoskeletal mechanics: atomic force microscopy force mapping of pulmonary endothelial monolayer. Nanomedicine **5:** 30–41

Blachutzik JO, Demir F, Kreuzer I, Hedrich R, Harms GS (2012) Methods of staining and visualization of sphingolipid enriched and non-enriched plasma membrane regions of *Arabidopsis thaliana* with fluorescent dyes and lipid analogues. Plant Methods **8:** 28

Bloom M, Evans E, Mouritsen OG (1991) Physical properties of the fluid lipid-bilayer component of cell membranes: a perspective. Q Rev Biophys **24:** 293–397

Bonneau L, Gerbeau-Pissot P, Thomas D, Der C, Lherminier J, Bourque S, Roche Y, Simon-Plas F (2010) Plasma membrane sterol complexation, generated by filipin, triggers signaling responses in tobacco cells. Biochim Biophys Acta **1798:** 2150–2159

Borner GH, Sherrier DJ, Weimar T, Michaelson LV, Hawkins ND, Macaskill A, Napier JA, Beale MH, Lilley KS, Dupree P (2005) Analysis of detergent-resistant membranes in Arabidopsis: evidence for plasma membrane lipid rafts. Plant Physiol **137:** 104–116

Chinchilla D, Zipfel C, Robatzek S, Kemmerling B, Nürnberger T, Jones JD, Felix G, Boller T (2007) A flagellin-induced complex of the receptor FLS2 and BAK1 initiates plant defence. Nature **448:** 497–500

de la Haba C, Palacio JR, Martinez P, Morros A (2013) Effect of oxidative stress on plasma membrane fluidity of THP-1 induced macrophages. Biochim Biophys Acta **1828:** 357–364

Demchenko AP, Mély Y, Duportail G, Klymchenko AS (2009) Monitoring biophysical properties of lipid membranes by environment-sensitive fluorescent probes. Biophys J **96:** 3461–3470

Demir F, Horntrich C, Blachutzik JO, Scherzer S, Reinders Y, Kierszniowska S, Schulze WX, Harms GS, Hedrich R, Geiger D, et al (2013) Arabidopsis nanodomain-delimited ABA signaling pathway regulates the anion channel SLAH3. Proc Natl Acad Sci USA **110:** 8296–8301

Denoux C, Galletti R, Mammarella N, Gopalan S, Werck D, De Lorenzo G, Ferrari S, Ausubel FM, Dewdney J (2008) Activation of defense response pathways by OGs and Flg22 elicitors in Arabidopsis seedlings. Mol Plant **1:** 423–445

Dinic J, Biverståhl H, Mäler L, Parmryd I (2011) Laurdan and di-4-ANEPPDHQ do not respond to membrane-inserted peptides and are good probes for lipid packing. Biochim Biophys Acta **1808:** 298–306

Duggan J, Jamal G, Tilley M, Davis B, McKenzie G, Vere K, Somekh MG, O'Shea P, Harris H (2008) Functional imaging of microdomains in cell membranes. Eur Biophys J **37:** 1279–1289

El Kirat K, Morandat S, Dufrêne YF (2010) Nanoscale analysis of supported lipid bilayers using atomic force microscopy. Biochim Biophys Acta **1798:** 750–765

Elmayan T, Fromentin J, Riondet C, Alcaraz G, Blein JP, Simon-Plas F (2007) Regulation of reactive oxygen species production by a 14-3-3 protein in elicited tobacco cells. Plant Cell Environ **30:** 722–732

Fujita A, Cheng J, Hirakawa M, Furukawa K, Kusunoki S, Fujimoto T (2007) Gangliosides GM1 and GM3 in the living cell membrane form clusters susceptible to cholesterol depletion and chilling. Mol Biol Cell **18:** 2112–2122

Furt F, König S, Bessoule JJ, Sargueil F, Zallot R, Stanislas T, Noirot E, Lherminier J, Simon-Plas F, Heilmann I, et al (2010) Polyphosphoinositides are enriched in plant membrane rafts and form microdomains in the plasma membrane. Plant Physiol **152:** 2173–2187

Garcia-Brugger A, Lamotte O, Vandelle E, Bourque S, Lecourieux D, Poinssot B, Wendehenne D, Pugin A (2006) Early signaling events induced by elicitors of plant defenses. Mol Plant Microbe Interact **19:** 711–724

García-Sáez AJ, Schwille P (2010) Stability of lipid domains. FEBS Lett **584:** 1653–1658

Gaus K, Chklovskaia E, Fazekas de St Groth B, Jessup W, Harder T (2005) Condensation of the plasma membrane at the site of T lymphocyte activation. J Cell Biol **171:** 121–131

Gaus K, Gratton E, Kable EP, Jones AS, Gelissen I, Kritharides L, Jessup W (2003) Visualizing lipid structure and raft domains in living cells with two-photon microscopy. Proc Natl Acad Sci USA **100:** 15554–15559

Gaus K, Zech T, Harder T (2006) Visualizing membrane microdomains by Laurdan 2-photon microscopy. Mol Membr Biol **23:** 41–48

Gerken JB, Chen JY, Massé RC, Powell AB, Stahl SS (2012) Development of an O_2-sensitive fluorescence-quenching assay for the combinatorial discovery of electrocatalysts for water oxidation. Angew Chem Int Ed Engl **51:** 6676–6680

Gielen E, Smisdom N, vandeVen M, De Clercq B, Gratton E, Digman M, Rigo JM, Hofkens J, Engelborghs Y, Ameloot M (2009) Measuring diffusion of lipid-like probes in artificial and natural membranes by raster image correlation spectroscopy (RICS): use of a commercial laser-scanning microscope with analog detection. Langmuir **25:** 5209–5218

Giocondi MC, Yamamoto D, Lesniewska E, Milhiet PE, Ando T, Le Grimellec C (2010) Surface topography of membrane domains. Biochim Biophys Acta **1798:** 703–718

Gómez-Gómez E, Boller T (2002) Flagellin perception: a paradigm for innate immunity. Trends Plant Sci **7:** 251–256

Gómez-Gómez E, Ruíz-Roldán MC, Di Pietro A, Roncero MI, Hera C (2002) Role in pathogenesis of two endo-β-1,4-xylanase genes from the vascular wilt fungus *Fusarium oxysporum*. Fungal Genet Biol **35:** 213–222

Guan X, Buchholz G, Nick P (2013) The cytoskeleton is disrupted by the bacterial effector HrpZ, but not by the bacterial PAMP flg22, in tobacco BY-2 cells. J Exp Bot **64:** 1805–1816

Heberle FA, Wu J, Goh SL, Petruzielo RS, Feigenson GW (2010) Comparison of three ternary lipid bilayer mixtures: FRET and ESR reveal nanodomains. Biophys J **99:** 3309–3318

Heiner AL, Gibbons E, Fairbourn JL, Gonzalez LJ, McLemore CO, Brueseke TJ, Judd AM, Bell JD (2008) Effects of cholesterol on physical properties of human erythrocyte membranes: impact on susceptibility to hydrolysis by secretory phospholipase A2. Biophys J **94:** 3084–3093

Ianoul A, Grant DD, Rouleau Y, Bani-Yaghoub M, Johnston LJ, Pezacki JP (2005) Imaging nanometer domains of β-adrenergic receptor complexes on the surface of cardiac myocytes. Nat Chem Biol **1:** 196–202

Jin L, Millard AC, Wuskell JP, Clark HA, Loew LM (2005) Cholesterol-enriched lipid domains can be visualized by di-4-ANEPPDHQ with linear and nonlinear optics. Biophys J **89:** L04–L06

Jin L, Millard AC, Wuskell JP, Dong X, Wu D, Clark HA, Loew LM (2006) Characterization and application of a new optical probe for membrane lipid domains. Biophys J **90:** 2563–2575

Jones JD, Dangl JL (2006) The plant immune system. Nature **444:** 323–329

Keinath NF, Kierszniowska S, Lorek J, Bourdais G, Kessler SA, Shimosato-Asano H, Grossniklaus U, Schulze WX, Robatzek S, Panstruga R (2010) PAMP (pathogen-associated molecular pattern)-induced changes in plasma membrane compartmentalization reveal novel components of plant immunity. J Biol Chem 285: 39140–39149

Kierszniowska S, Seiwert B, Schulze WX (2009) Definition of Arabidopsis sterol-rich membrane microdomains by differential treatment with methyl-β-cyclodextrin and quantitative proteomics. Mol Cell Proteomics 8: 612–623

Klausner RD, Wolf DE (1980) Selectivity of fluorescent lipid analogues for lipid domains. Biochemistry 19: 6199–6203

Klenerman D, Korchev YE, Davis SJ (2011) Imaging and characterisation of the surface of live cells. Curr Opin Chem Biol 15: 696–703

Klymchenko AS, Oncul S, Didier P, Schaub E, Bagatolli L, Duportail G, Mély Y (2009) Visualization of lipid domains in giant unilamellar vesicles using an environment-sensitive membrane probe based on 3-hydroxyflavone. Biochim Biophys Acta 1788: 495–499

Königshofer H, Tromballa HW, Löppert HG (2008) Early events in signalling high-temperature stress in tobacco BY2 cells involve alterations in membrane fluidity and enhanced hydrogen peroxide production. Plant Cell Environ 31: 1771–1780

Konopka CA, Backues SK, Bednarek SY (2008) Dynamics of Arabidopsis dynamin-related protein 1C and a clathrin light chain at the plasma membrane. Plant Cell 20: 1363–1380

Kress A, Ferrand P, Rigneault H, Trombik T, He HT, Marguet D, Brasselet S (2011) Probing orientational behavior of MHC class I protein and lipid probes in cell membranes by fluorescence polarization-resolved imaging. Biophys J 101: 468–476

Kubiak J, Brewer J, Hansen S, Bagatolli LA (2011) Lipid lateral organization on giant unilamellar vesicles containing lipopolysaccharides. Biophys J 100: 978–986

Kucherak OA, Oncul S, Darwich Z, Yushchenko DA, Arntz Y, Didier P, Mély Y, Klymchenko AS (2010) Switchable nile red-based probe for cholesterol and lipid order at the outer leaflet of biomembranes. J Am Chem Soc 132: 4907–4916

Laloi M, Perret AM, Chatre L, Melser S, Cantrel C, Vaultier MN, Zachowski A, Bathany K, Schmitter JM, Vallet M, et al (2007) Insights into the role of specific lipids in the formation and delivery of lipid microdomains to the plasma membrane of plant cells. Plant Physiol 143: 461–472

Leborgne-Castel N, Lherminier J, Der C, Fromentin J, Houot V, Simon-Plas F (2008) The plant defense elicitor cryptogein stimulates clathrin-mediated endocytosis correlated with reactive oxygen species production in bright yellow-2 tobacco cells. Plant Physiol 146: 1255–1266

Lecourieux D, Lamotte O, Bourque S, Wendehenne D, Mazars C, Ranjeva R, Pugin A (2005) Proteinaceous and oligosaccharidic elicitors induce different calcium signatures in the nucleus of tobacco cells. Cell Calcium 38: 527–538

Lecourieux D, Mazars C, Pauly N, Ranjeva R, Pugin A (2002) Analysis and effects of cytosolic free calcium increases in response to elicitors in Nicotiana plumbaginifolia cells. Plant Cell 14: 2627–2641

Lefebvre B, Furt F, Hartmann MA, Michaelson LV, Carde JP, Sargueil-Boiron F, Rossignol M, Napier JA, Cullimore J, Bessoule JJ, et al (2007) Characterization of lipid rafts from Medicago truncatula root plasma membranes: a proteomic study reveals the presence of a raft-associated redox system. Plant Physiol 144: 402–418

Lherminier J, Elmayan T, Fromentin J, Elaraqui KT, Vesa S, Morel J, Verrier JL, Cailleteau B, Blein JP, Simon-Plas F (2009) NADPH oxidase-mediated reactive oxygen species production: subcellular localization and reassessment of its role in plant defense. Mol Plant Microbe Interact 22: 868–881

Li Y, Martin BR, Cravatt BF, Hofmann SL (2012) DHHC5 protein palmitoylates flotillin-2 and is rapidly degraded on induction of neuronal differentiation in cultured cells. J Biol Chem 287: 523–530

Lichtenberg D, Goñi FM, Heerklotz H (2005) Detergent-resistant membranes should not be identified with membrane rafts. Trends Biochem Sci 30: 430–436

Lingwood D, Ries J, Schwille P, Simons K (2008) Plasma membranes are poised for activation of raft phase coalescence at physiological temperature. Proc Natl Acad Sci USA 105: 10005–10010

Lingwood D, Simons K (2010) Lipid rafts as a membrane-organizing principle. Science 327: 46–50

Liu P, Li RL, Zhang L, Wang QL, Niehaus K, Baluska F, Samaj J, Lin JX (2009) Lipid microdomain polarization is required for NADPH oxidase-dependent ROS signaling in Picea meyeri pollen tube tip growth. Plant J 60: 303–313

Los DA, Murata N (2004) Membrane fluidity and its roles in the perception of environmental signals. Biochim Biophys Acta 1666: 142–157

Luu DT, Martinière A, Sorieul M, Runions J, Maurel C (2012) Fluorescence recovery after photobleaching reveals high cycling dynamics of plasma membrane aquaporins in Arabidopsis roots under salt stress. Plant J 69: 894–905

M'Baye G, Mély Y, Duportail G, Klymchenko AS (2008) Liquid ordered and gel phases of lipid bilayers: fluorescent probes reveal close fluidity but different hydration. Biophys J 95: 1217–1225

Miguel L, Owen DM, Lim C, Liebig C, Evans J, Magee AI, Jury EC (2011) Primary human CD4+ T cells have diverse levels of membrane lipid order that correlate with their function. J Immunol 186: 3505–3516

Mongrand S, Morel J, Laroche S, Claverol S, Carde JP, Hartmann MA, Bonneu M, Simon-Plas F, Lessire R, Bessoule JJ (2004) Lipid rafts in higher plant cells: purification and characterization of Triton X-100-insoluble microdomains from tobacco plasma membrane. J Biol Chem 279: 36277–36286

Mongrand S, Stanislas T, Bayer EM, Lherminier J, Simon-Plas F (2010) Membrane rafts in plant cells. Trends Plant Sci 15: 656–663

Morel J, Claverol S, Mongrand S, Furt F, Fromentin J, Bessoule JJ, Blein JP, Simon-Plas F (2006) Proteomics of plant detergent-resistant membranes. Mol Cell Proteomics 5: 1396–1411

Nagy E, Balogi Z, Gombos I, Akerfelt M, Björkbom A, Balogh G, Török Z, Maslyanko A, Fiszer-Kierzkowska A, Lisowska K, et al (2007) Hyperfluidization-coupled membrane microdomain reorganization is linked to activation of the heat shock response in a murine melanoma cell line. Proc Natl Acad Sci USA 104: 7945–7950

Nourissat P, Travert M, Chevanne M, Tekpli X, Rebillard A, Le Moigne-Müller M, Rissel M, Cillard J, Dimanche-Boitrel MT, Lagadic-Gossmann D, et al (2008) Ethanol induces oxidative stress in primary rat hepatocytes through the early involvement of lipid raft clustering. Hepatology 47: 59–70

Oncul S, Klymchenko AS, Kucherak OA, Demchenko AP, Martin S, Dontenwill M, Arntz Y, Didier P, Duportail G, Mély Y (2010) Liquid ordered phase in cell membranes evidenced by a hydration-sensitive probe: effects of cholesterol depletion and apoptosis. Biochim Biophys Acta 1798: 1436–1443

Orth A, Johannes L, Römer W, Steinem C (2012) Creating and modulating microdomains in pore-spanning membranes. ChemPhysChem 13: 108–114

Owen DM, Gaus K, Magee AI, Cebecauer M (2010a) Dynamic organization of lymphocyte plasma membrane: lessons from advanced imaging methods. Immunology 131: 1–8

Owen DM, Lanigan PM, Dunsby C, Munro I, Grant D, Neil MA, French PM, Magee AI (2006) Fluorescence lifetime imaging provides enhanced contrast when imaging the phase-sensitive dye di-4-ANEPPDHQ in model membranes and live cells. Biophys J 90: L80–L82

Owen DM, Magenau A, Majumdar A, Gaus K (2010b) Imaging membrane lipid order in whole, living vertebrate organisms. Biophys J 99: L7–L9

Owen DM, Oddos S, Kumar S, Davis DM, Neil MA, French PM, Dustin ML, Magee AI, Cebecauer M (2010c) High plasma membrane lipid order imaged at the immunological synapse periphery in live T cells. Mol Membr Biol 27: 178–189

Owen DM, Rentero C, Magenau A, Abu-Siniyeh A, Gaus K (2012a) Quantitative imaging of membrane lipid order in cells and organisms. Nat Protoc 7: 24–35

Owen DM, Williamson D, Magenau A, Gaus K (2012b) Optical techniques for imaging membrane domains in live cells (live-cell palm of protein clustering). Methods Enzymol 504: 221–235

Parasassi T, De Stasio G, d'Ubaldo A, Gratton E (1990) Phase fluctuation in phospholipid membranes revealed by Laurdan fluorescence. Biophys J 57: 1179–1186

Parton RG, Hancock JF (2004) Lipid rafts and plasma membrane microorganization: insights from Ras. Trends Cell Biol 14: 141–147

Pike LJ (2006) Rafts defined: a report on the Keystone Symposium on Lipid Rafts and Cell Function. J Lipid Res 47: 1597–1598

Ponchet M, Panabières F, Mikes V, Montillet JL, Suty L, Triantaphylides C, Tirilly Y, Blein JP, Milat ML (1999) Are elicitins cryptograms in plant-oomycete communications? Cell Mol Life Sci 56: 1020–1047

Raffaele S, Bayer E, Lafarge D, Cluzet S, German Retana S, Boubekeur T, Leborgne-Castel N, Carde JP, Lherminier J, Noirot E, et al (2009)

Remorin, a Solanaceae protein resident in membrane rafts and plasmodesmata, impairs *Potato virus X* movement. Plant Cell **21:** 1541–1555

Ricci P, Bonnet P, Huet JC, Sallantin M, Beauvais-Cante F, Bruneteau M, Billard V, Michel G, Pernollet JC (1989) Structure and activity of proteins from pathogenic fungi *Phytophthora* eliciting necrosis and acquired resistance in tobacco. Eur J Biochem **183:** 555–563

Rilfors L, Lindblom G, Wieslander A, Christiansson A (1984) Lipid bilayer stability in biological membranes. *In* M Kates, LA Manson, eds, Biomembranes, Vol 12. Plenum Press, New York, pp 205–245

Rinia HA, de Kruijff B (2001) Imaging domains in model membranes with atomic force microscopy. FEBS Lett **504:** 194–199

Roche Y, Gerbeau-Pissot P, Buhot B, Thomas D, Bonneau L, Gresti J, Mongrand S, Perrier-Cornet JM, Simon-Plas F (2008) Depletion of phytosterols from the plant plasma membrane provides evidence for disruption of lipid rafts. FASEB J **22:** 3980–3991

Roche Y, Klymchenko AS, Gerbeau-Pissot P, Gervais P, Mély Y, Simon-Plas F, Perrier-Cornet JM (2010) Behavior of plant plasma membranes under hydrostatic pressure as monitored by fluorescent environment-sensitive probes. Biochim Biophys Acta **1798:** 1601–1607

Rosetti CM, Maggio B, Wilke N (2010) Micron-scale phase segregation in lipid monolayers induced by myelin basic protein in the presence of a cholesterol analog. Biochim Biophys Acta **1798:** 498–505

Sengupta P, Hammond A, Holowka D, Baird B (2008) Structural determinants for partitioning of lipids and proteins between coexisting fluid phases in giant plasma membrane vesicles. Biochim Biophys Acta **1778:** 20–32

Sergent O, Pereira M, Belhomme C, Chevanne M, Huc L, Lagadic-Gossmann D (2005) Role for membrane fluidity in ethanol-induced oxidative stress of primary rat hepatocytes. J Pharmacol Exp Ther **313:** 104–111

Simon-Plas F, Perraki A, Bayer E, Gerbeau-Pissot P, Mongrand S (2011) An update on plant membrane rafts. Curr Opin Plant Biol **14:** 642–649

Simons K, Gerl MJ (2010) Revitalizing membrane rafts: new tools and insights. Nat Rev Mol Cell Biol **11:** 688–699

Simons K, Ikonen E (1997) Functional rafts in cell membranes. Nature **387:** 569–572

Simons K, Sampaio JL (2011) Membrane organization and lipid rafts. Cold Spring Harb Perspect Biol **3:** a004697

Sorek N, Gutman O, Bar E, Abu-Abied M, Feng X, Running MP, Lewinsohn E, Ori N, Sadot E, Henis YI, et al (2011) Differential effects of prenylation and *S*-acylation on type I and II ROPS membrane interaction and function. Plant Physiol **155:** 706–720

Stanislas T, Bouyssie D, Rossignol M, Vesa S, Fromentin J, Morel J, Pichereaux C, Monsarrat B, Simon-Plas F (2009) Quantitative proteomics reveals a dynamic association of proteins to detergent-resistant membranes upon elicitor signaling in tobacco. Mol Cell Proteomics **8:** 2186–2198

Stöckl MT, Herrmann A (2010) Detection of lipid domains in model and cell membranes by fluorescence lifetime imaging microscopy. Biochim Biophys Acta **1798:** 1444–1456

van der Meer W, Pottel H, Herreman W, Ameloot M, Hendrickx H, Schröder H (1984) Effect of orientational order on the decay of the fluorescence anisotropy in membrane suspensions. A new approximate solution of the rotational diffusion equation. Biophys J **46:** 515–523

Vaultier MN, Cantrel C, Vergnolle C, Justin AM, Demandre C, Benhassaine-Kesri G, Çiçek D, Zachowski A, Ruelland E (2006) Desaturase mutants reveal that membrane rigidification acts as a cold perception mechanism upstream of the diacylglycerol kinase pathway in Arabidopsis cells. FEBS Lett **580:** 4218–4223

Veatch SL, Keller SL (2005) Seeing spots: complex phase behavior in simple membranes. Biochim Biophys Acta **1746:** 172–185

Vereb G, Matkó J, Vámosi G, Ibrahim SM, Magyar E, Varga S, Szöllosi J, Jenei A, Gáspár R Jr, Waldmann TA, et al (2000) Cholesterol-dependent clustering of IL-2Rα and its colocalization with HLA and CD48 on T lymphoma cells suggest their functional association with lipid rafts. Proc Natl Acad Sci USA **97:** 6013–6018

Verstraeten SV, Mackenzie GG, Oteiza PI (2010) The plasma membrane plays a central role in cells response to mechanical stress. Biochim Biophys Acta **1798:** 1739–1749

Vígh L, Török Z, Balogh G, Glatz A, Piotto S, Horváth I (2007) Membrane-regulated stress response: a theoretical and practical approach. Adv Exp Med Biol **594:** 114–131

Wesołowska O, Michalak K, Maniewska J, Hendrich AB (2009) Giant unilamellar vesicles: a perfect tool to visualize phase separation and lipid rafts in model systems. Acta Biochim Pol **56:** 33–39

Wheeler G, Tyler KM (2011) Widefield microscopy for live imaging of lipid domains and membrane dynamics. Biochim Biophys Acta **1808:** 634–641

Winckler P, Cailler A, Deturche R, Jeannesson P, Morjani H, Jaffiol R (2012) Microfluidity mapping using fluorescence correlation spectroscopy: a new way to investigate plasma membrane microorganization of living cells. Biochim Biophys Acta **1818:** 2477–2485

Zappel NF, Panstruga R (2008) Heterogeneity and lateral compartmentalization of plant plasma membranes. Curr Opin Plant Biol **11:** 632–640